

1 **Two-Stage Aerosol Formation in Low-Temperature Combustion**

2 El Hajj, O.^a, Atwi, K.^a, Cheng, Z.^a, Koritzke, A.L.^b, Christianson, M.G.^b, Dewey, N.S.^b, Rotavera, B.^{a,b*}, Saleh,
3 R.^{a*}

4 ^aSchool of Environmental, Civil, Agricultural, and Mechanical Engineering, University of Georgia, Athens,
5 Georgia, USA

6 ^bDepartment of Chemistry, University of Georgia, Athens, Georgia, USA

7 * *To whom correspondence should be addressed:* rawad@uga.edu, rotavera@uga.edu

8 **Abstract**

9 Low-temperature combustion is a promising strategy for reducing pollutant formation in internal
10 combustion engines. However, there is a lack of understanding of how the chemistry governing the
11 differences in ignition between low-temperature and conventional combustion affects the emission rates
12 and physicochemical properties of particulate matter (aerosols). Here, we conducted combustion
13 experiments in an atmospheric-pressure reactor controlled at constant equivalence ratio ($\phi = 2.3$) and
14 $O_2/N_2 = 0.06$, and at temperatures varied between 200 °C and 1035 °C. We used two fuels: toluene,
15 which has high sooting propensity, and *n*-heptane, which has a comparatively lower sooting propensity
16 but exhibits two-stage ignition that is not present in toluene combustion. We performed real-time
17 measurements of aerosol size distributions, volatility, and light-absorption properties. We also
18 performed offline molecular-size characterization. Aerosols emitted from both fuels were comprised of
19 light-absorbing organics that are categorized as brown carbon. At the highest combustion temperature
20 (1035 °C), the aerosol emissions from toluene combustion were a factor of 20 larger than *n*-heptane.
21 The aerosol emissions from toluene combustion had more abundance of large molecular-size species,
22 were less volatile, and were more light-absorbing than *n*-heptane. For both fuels, aerosol emission
23 factors exhibited a steep drop with decreasing temperatures. However, there was a resurgence in aerosol
24 emissions at lower temperatures with a peak at 290 °C for *n*-heptane combustion that was not observed
25 for toluene. This is consistent with chemical kinetics simulations that show prominent two-stage
26 ignition behavior for *n*-heptane, but not for toluene.

27 **1. Introduction**

28 Advanced compression-ignition (ACI) is a next-generation strategy in internal combustion engines
29 that aims to achieve high efficiency while maintaining low levels of pollution emissions [1-3]. Several
30 ACI technologies have been proposed, including homogeneous charge compression-ignition (HCCI),
31 premixed charge compression ignition (PCCI) [4-7], and reactivity controlled compression-ignition
32 (RCCI) [8, 9], as well as hybrid concepts that combine different ACI strategies [10, 11]. All these
33 approaches rely on low-temperature combustion (LTC) to reduce pollutant emissions by avoiding the
34 NOx-soot tradeoff that occurs at the combustion conditions typical for conventional diesel combustion
35 (CDC) [12, 13]. The widely accepted model [14] is that NOx forms at high temperatures ($T > 1900$ °C)
36 and fuel-lean conditions (equivalence ratio, $\phi < 1$) while soot forms at relatively lower temperatures (T
37 ≈ 1100 °C – 1700 °C) and fuel-rich conditions ($\phi > 2$). CDC systems involve inhomogeneous
38 combustion conditions with respect to fuel/air mixing and temperature. As a result, conditions in those
39 systems span both the soot- and NOx-formation regions. Any alterations to engine operation within the
40 CDC environment would push the conditions further into one of these two regions, hence the NOx-soot
41 tradeoff [3]. On the other hand, the premixing and ignition delay employed in LTC engines allow for a
42 more homogeneous fuel-lean combustion at temperatures substantially lower than CDC, thus avoiding
43 both soot and NOx formation regions. Given the strong dependence of NOx formation on combustion
44 temperature, its near-elimination in LTC is certain. However, the elimination of soot formation in LTC
45 is not as straightforward.

46 The terminology concerning aerosols, or particulate matter, in combustion emissions can be
47 confusing. Therefore, it is important to explain the terminology that we adopt in this paper. In
48 combustion engines literature, and to a certain extent in atmospheric science literature, the term “soot”
49 is used to represent aerosol combustion emissions that are comprised of solid aggregates of elemental
50 carbon (EC). EC is also often used synonymously with black carbon (BC) in the atmospheric science
51 literature due to its black appearance (strong light absorption in the visible spectrum) [15]. However,
52 depending on the combustion conditions, a significant fraction of aerosol combustion emissions can be
53 organic and is referred to as organic aerosol (OA) or organic carbon (OC) (i.e. when only accounting

54 for the carbon content of the organic molecules). In fact, OA can form through the same soot-formation
55 route as EC, which involves growth and aggregation of polycyclic aromatic hydrocarbons (PAHs) [16,
56 17] but under conditions that are not conducive for the completion of the soot-formation process. To
57 emphasize this connection, Michelsen [17] refers to this OA as “incipient soot” and the solid aggregates,
58 mostly EC aerosols as “mature soot.” In this paper, we adopt the Michelsen terminology, and hereafter,
59 we add (mature) before “soot” when referencing previous studies to emphasize that what those studies
60 refer to as “soot” is indeed “mature soot.” We have shown that incipient soot comprises a major fraction
61 of atmospheric brown carbon (BrC) [18]. BrC, or light-absorbing OA, is less absorptive than BC in the
62 visible spectrum and exhibits absorption more skewed toward the short wavelengths, which gives it its
63 brown color [19, 20]. BC, mostly comprised of elemental carbon, has relatively constrained light-
64 absorption properties while BrC is comprised of a multitude of organic species with light-absorption
65 efficiencies that vary over several orders of magnitude [21, 22]. BrC plays an important role alongside
66 BC in absorbing solar radiation and climate forcing [21, 22]. For completeness, we note that OA in
67 combustion-engine emissions also includes organic species other than incipient soot (e.g. from
68 lubricating oil [23]), and altogether, OA emissions from combustion are referred to as primary organic
69 aerosol (POA). For readers not familiar with aerosol terminology, we summarize the key definitions
70 discussed in this paragraph in Table 1.

71 **Table 1.** Summary of definitions of key terms related to combustion aerosols

Term	Definition
Mature soot [17]	<ul style="list-style-type: none">- Solid aggregates of mostly elemental carbon emitted from incomplete combustion.- Often referred to as just “soot” in both combustion and atmospheric science literature.
Incipient soot [17]	<ul style="list-style-type: none">- Organic aerosol emitted from incomplete combustion that form through the same soot-formation route as mature soot but under conditions (e.g. low temperature) not conducive for the completion of the soot-formation process.- Is categorized as POA.- Can be light-absorbing and thus categorized as brown carbon (BrC)

Black carbon (BC) [15]	<ul style="list-style-type: none"> - Comprised mostly of elemental carbon, it is defined operationally based on its black appearance (strong light absorption in the visible spectrum). - Its definition largely overlaps with that of mature soot.
Brown carbon (BrC) [20]	<ul style="list-style-type: none"> - Light-absorbing organic aerosol (OA). - Defined operationally based on its light-absorption properties that exhibit strong wavelength dependence in the visible spectrum (increased absorption toward short wavelengths), thus giving it a brown appearance.

72

73 Previous studies have reported substantial decrease of (mature) soot production in engines [9, 24-
 74 29] and constant-volume combustion chambers [30, 31] operated in LTC mode versus CDC mode.
 75 However, these reports are based on optical techniques that are tailored for measuring CDC aerosol
 76 emissions, which are dominated by mature soot. The most common method is the filter smoke number
 77 (FSN) obtained from reflectance measurements of particles collected on a filter [28, 29, 32, 33]. Other
 78 techniques include the commercially available Opacimeter [24] and Micro Soot Sensor [25, 34], as well
 79 as other light-extinction techniques (e.g. forward illumination light extinction) [30]. All these
 80 techniques exploit the strong light-absorptive nature of mature soot and convert the observed light
 81 absorption into particle mass based on either calibration against or assumed light-absorption properties
 82 of mature soot (or BC). Because LTC emissions are dominated by OC, which is significantly less
 83 absorptive than EC [2], these techniques would severely underestimate the mass loadings of aerosols
 84 emitted under LTC conditions [32].

85 Realizing that the aerosol emissions in LTC are dominated by OA, several studies have applied
 86 aerosol characterization techniques that do not rely on light absorption and are therefore not specific
 87 for mature soot. Northrop et al. [35] showed that even though the production of EC (i.e. mature soot)
 88 was largely reduced in LTC of biodiesel, the emissions contained considerable amounts of OA that
 89 were characterized using electrical mobility measurements. Lucachick et al. [36] reported that the
 90 aerosol emissions in LTC (PCCI and RCCI) contained substantially less (mature) soot than CDC and
 91 were dominated by semi-volatile OA, as shown by volatility tandem differential mobility analysis.
 92 Storey et al. [32] reported that while the FSN method predicted negligible aerosol emissions from an

93 engine operated in RCCI mode compared to CDC mode, gravimetric analysis showed that the mass
94 loadings of aerosol emissions from the two modes were of the same order of magnitude. Moses-DeBusk
95 et al. [2] reported that the aerosol emissions from an engine operated at HCCI conditions were
96 dominated by OA, as obtained using an OC-EC analyzer. Consequently, the aerosol mass emission rate
97 measured using a Micro Soot Sensor was an order of magnitude smaller than that measured using the
98 OC-EC analyzer, emphasizing the inadequacy of instruments tailored to detect mature soot at
99 quantifying LTC aerosol emissions.

100 The studies summarized above demonstrate that LTC suppresses (mature) soot production but it can
101 potentially lead to significant OA production. However, while the framework for the chemistry
102 governing autoignition at LTC conditions is well understood as a degenerate chain-branching
103 mechanism [37], the dependence of aerosol emission rates and their physicochemical properties on
104 combustion temperature within LTC conditions is not. In this study, we performed controlled-
105 combustion experiments at temperatures relevant for LTC conditions (≤ 1035 °C) and quantified the
106 aerosol emissions and characterized their molecular sizes, volatility, and light-absorption properties.
107 The experiments involved two structurally different fuels (toluene and *n*-heptane) in order to investigate
108 the effect of differences in fuel reactivity on the emitted aerosols.

109 **2. Materials and Methods**

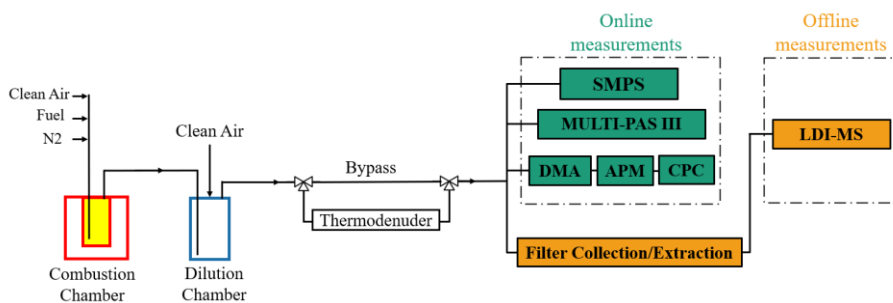
110 2.1. Approach

111 The suppression of mature soot (EC) and elevated levels OA in LTC compared to CDC can be
112 understood within the context of the soot-formation process in combustion. The initial steps of the
113 process involve the formation of small aromatic species, which then aggregate to form polycyclic
114 aromatic hydrocarbons (PAHs) [16]. Aided by radical chain reactions, PAHs and other available
115 hydrocarbons cluster to form condensable organic particles [38], or incipient soot [17]. These organic
116 particles then undergo progressive dehydrogenation and aggregation to eventually form the EC
117 aggregates that comprise mature soot [17]. While the combustion conditions in CDC promote the
118 generation of mature soot, it is plausible that the low temperatures in LTC are not conducive for the

119 completion of the soot-formation process (i.e. complete soot maturation), thus leading to the production
120 of organic incipient soot. We have previously shown that incipient soot (or BrC) exhibits wide
121 variability in physicochemical properties (molecular sizes, volatility, and light-absorption properties)
122 [18, 39-41] depending on combustion conditions. Here, we isolate the effect of temperature.

123 We performed controlled-combustion experiments at constant pressure (1 atm), equivalence ratio (ϕ
124 = 2.3), and oxygen-to-nitrogen ratio ($O_2/N_2 = 0.06$), and varied the temperature between 250 °C and
125 1035 °C. This temperature range covers the lower end of in-cylinder temperatures encountered in LTC
126 conditions, which are typically between 700 °C and 1700 °C [3]. It also encompasses exhaust
127 temperatures, which range from 120 °C to 400 °C [42, 43], where unburned fuel can continue to react.
128 These low temperatures are also representative of “cold start” conditions in conventional engines,
129 during which the majority of aerosol emissions take place over a typical driving cycle [44]. We
130 investigated the effect of molecular structure by performing the experiments with two structurally
131 different fuels that have been previously utilized in LTC studies: *n*-heptane [45, 46] and toluene [45,
132 47-52].

133 In each experiment, we performed online measurements to characterize the emission factors, size
134 distributions, volatility, and light-absorption properties of the emitted aerosols. We also collected filters
135 for offline chemical characterization using laser desorption ionization mass spectrometry (LDI-MS).
136 The experimental setup is shown in Figure 1 and the associated measurements are described in detail
137 in the subsequent subsections. To complement the experiments, species profiles of *n*-heptane, toluene,
138 and several intermediates were simulated using the chemical kinetics mechanism of Mehl et al. [53].



139
140 **Figure 1.** Schematic of the experimental setup

141 2.2. Combustion system

142 The combustion experiments were performed using a custom-built controlled-combustion system
143 [18, 39, 40, 54]. It consists of a custom-made cylindrical quartz chamber (~0.24 L) enclosed in a heater
144 (Thermcraft). The combustion reaction is temperature-initiated. A PID controller (OMEGA, CNi3244)
145 controls the wattage of the heater to achieve a set combustion temperature measured at the center of the
146 combustion chamber using a high-temperature K-type thermocouple. In this study, we controlled the
147 temperature in the combustion chamber to set values between 250 °C and 1035 °C. Fuel is introduced
148 into the combustion chamber in vapor form by flowing a stream of clean dried air, controlled using a
149 mass flow controller (DAKOTA, 6AGC1AL55-09AB), into a bubbler containing the fuel. We have
150 previously performed mass transfer calculations and confirmed that the residence time of a bubble rising
151 in the bubbler is greater than the time required to saturate it with fuel [39]. Therefore, the flowrate of
152 the fuel exiting the bubbler can be calculated from knowledge of the fuel saturation pressure and the air
153 flowrate. We controlled the equivalence ratio ($\phi = 2.3$) and $O_2/N_2 = 0.06$ by mixing the fuel-saturated
154 air stream with a controlled stream of clean air and a controlled stream of N_2 . The values of the flowrates
155 are given in Table S1 in the Supplementary Material (SM).

156 2.3. Online measurements

157 We measured the electrical-mobility size distributions of the emitted aerosols at each combustion
158 temperature using a scanning mobility particle sizer (SMPS, TSI 3882) in the range of 10-500 nm. The
159 SMPS uses an electrostatic classifier (TSI, Model 3082), a long differential mobility analyzer (DMA,
160 TSI, Model 3081A00), and an advanced aerosol neutralizer (TSI, Model 3088) along with a
161 condensation particle counter (CPC, TSI, Model 3772). We also integrated the SMPS size distributions
162 in conjunction with particle effective densities to obtain total aerosol mass concentrations ($C_{aerosol}$). The
163 particle effective densities were obtained using the tandem differential mobility analyzer – aerosol
164 particle sizer (tandem DMA-APM) technique [55]. Particles were classified based on their electrical-
165 mobility diameter (d_m) using the DMA (TSI, Model 3081A00) and their mass (m_p) was measured using
166 the APM (Kanomax, Model 3601). The effective density was then calculated as:

167
$$\rho_{\text{eff}} = \frac{m_p}{v_p} ; v_p = \frac{\pi d_m^3}{6} \quad (1)$$

168 The uncertainties in d_m and m_p are < 1.5% [56] and < 5% [57], respectively. This leads to a propagated
 169 uncertainty of < 7% in ρ_{eff} . We obtained $\rho_{\text{eff}} = 1.3 \pm 0.09 \text{ g/cm}^3$ for emissions from both fuels, which is
 170 consistent with values typically reported for OA [39, 58, 59].

171 We calculated the aerosol emission factors per unit mass fuel as:

172
$$\text{EF} = \frac{C_{\text{aerosol}}}{C_{\text{fuel}}} \quad (2)$$

173 Where C_{fuel} is the mass concentration of the fuel entering the combustion chamber, calculated as:

174
$$C_{\text{fuel}} = \frac{Q_{\text{fuel}}}{Q_{\text{total}}} \quad (3)$$

175 Where Q_{fuel} is the fuel flowrate into the combustion chamber, Q_{total} is the total flowrate (fuel + air + N_2)
 176 (Figure 1), and M_{fuel} is the molar mass of the fuel.

177 We measured the absorption coefficients (b_{abs} , Mm^{-1}) at three wavelengths ($\lambda = 422, 532$, and 782
 178 nm) using a photoacoustic spectrophotometer (MULTI-PAS III) [60]. For aerosols, b_{abs} is an extensive
 179 property that represents the total light absorption cross-section of the particles per unit volume of air,
 180 and should not be confused with the absorption coefficient used in UV-vis spectroscopy, which has the
 181 same inverse length dimensions but represents absorbance per unit path length and is an intensive
 182 property. Normalizing b_{abs} by the total mass concentration of the particles (C_{aerosol}) yields the mass
 183 absorption cross-section (MAC, m^2/g):

184
$$\text{MAC}(\lambda) = \frac{b_{\text{abs}}(\lambda)}{C_{\text{aerosol}}} \quad (4)$$

185 MAC exhibits an inverse power-law dependence on λ with the exponent of the power-law known as
 186 the absorption Ångström exponent (AAE). MAC and AAE, are not true intensive properties as they
 187 depend on particle size and morphology, but they can be conveniently calculated from light-absorption
 188 and particle concentration measurements and are thus often used as effective light-absorption
 189 properties.

190 We also retrieved the fundamental light-absorption property of the aerosols, namely the imaginary
191 part of the refractive index (k) using optical closure [18, 40, 61]. We performed optical calculations
192 based on Mie theory [62] with the aerosol size distributions obtained from SMPS measurements as
193 model inputs and $k(\lambda)$ as a free parameter. We have previously shown that particles emitted at similar
194 conditions were liquid near-spherical particles based on scanning electron microscopy (SEM) imaging
195 [18], thus justifying the application of Mie theory. Therefore, the mobility equivalent We retrieved k
196 values from matching the calculated absorption coefficients ($b_{\text{abs,Mie}}(\lambda)$) to $b_{\text{abs}}(\lambda)$ measured using the
197 MULTI-PAS III. Similar to MAC, k also exhibits an inverse power-law dependence on λ with an
198 exponent w [22]. In the small particle limit ($d \ll \lambda$), $\text{AAE} \approx w + 1$ [22].

199 For select combustion-chamber temperatures, we sampled the emitted aerosols through a
200 thermodenuder to characterize their volatility. The thermodenuder is a stainless-steel tube ($L = 100$ cm,
201 ID = 2.5 cm) wrapped with heating wire that is controlled using a PID controller (OMEGA, CNi3244)
202 to maintain a set temperature measured at the centerline of the flow using a K-type thermocouple. In
203 this study, we applied 3 thermodenuder temperatures (50 °C, 100 °C, and 150 °C) and obtained the
204 aerosol mass fraction remaining (MFR) at each temperature as:

$$205 \quad \text{MFR} = C_{\text{aerosol,TD}} / C_{\text{aerosol,bypass}} \quad (5)$$

206 Where $C_{\text{aerosol,bypass}}$ is the original aerosol mass concentration and $C_{\text{aerosol,TD}}$ is the mass concentration
207 after heating in the TD (see Figure 1). Plots of MFR versus TD temperature, or thermograms, can be
208 used to compare the volatility of different aerosol samples, where a steeper thermogram indicates higher
209 volatility. We note that MFR is not a fundamental property as it depends on the initial aerosol mass
210 concentration (i.e. $C_{\text{aerosol,bypass}}$) [63]. Therefore, using thermograms to compare the volatility of different
211 aerosol population requires that $C_{\text{aerosol,bypass}}$ is the same. In this study, we ensured that $C_{\text{aerosol,bypass}}$ was
212 consistent (350 $\mu\text{g}/\text{m}^3$) across different experiments by applying controlled dilution to the emissions
213 downstream of the combustion chamber (Figure 1).

214 2.4. Offline chemical analysis

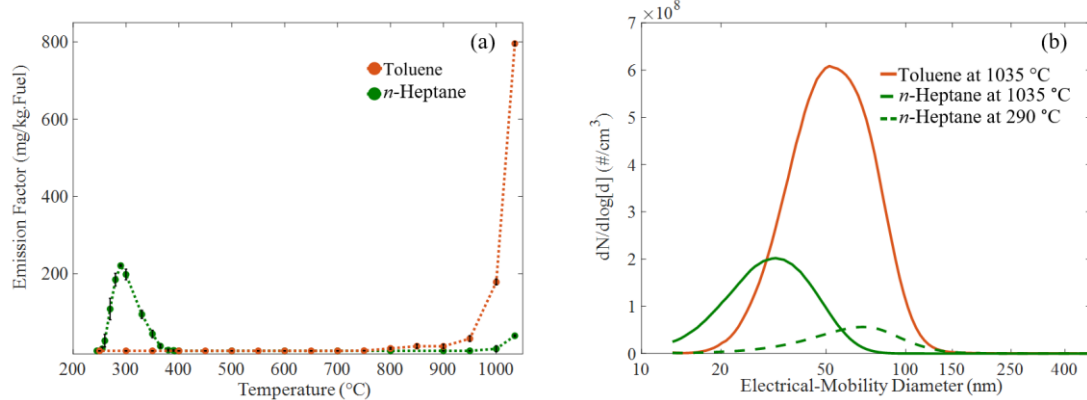
215 For select combustion-chamber temperatures, we collected aerosol samples for offline analysis using
216 laser desorption ionization mass spectrometry (LDI-MS). Aerosol samples were collected on 47 mm
217 Teflon filters (0.2 μ m pore size, Whatman) at a flowrate of 10 LPM. The targeted mass loading on the
218 filters was typically 300 μ g in order to avoid filter clogging which occurs at \sim 350 μ g. The filters were
219 then immersed in 10 ml dichloromethane (DCM) and sonicated for 40 minutes to extract the aerosol
220 samples. We spotted 10 μ l of the extracted solution on an LDI-MS plate and let the DCM evaporate
221 leaving the sample for analysis using a Bruker Autoflex TOF mass spectrometer operated in reflectron
222 mode. The instrument uses a 337 nm Nitrogen laser in positive mode. The ion source was set to 19 kV
223 and the reflector voltage to 20 kV. The spectrum for each sample was obtained as an average from 200
224 laser shots.

225 The advantage of LDI-MS is that it is soft-ionizing and thus allows for the detection of the large
226 molecules, including polycyclic aromatic hydrocarbons (PAHS) and their derivatives, that make up the
227 organic incipient soot particles [18, 61, 64-66]. We note that LDI-MS measurements are semi-
228 quantitative due to differences in desorption and ionization efficiencies between different molecules
229 that largely depend on the operating conditions [67]. However, one can make qualitative comparisons
230 between mass spectra of samples obtained under the same LDI-MS operating conditions.

231 **3. Results**

232 3.1. Emission factors and size distributions

233 Figure 2a depicts emission factors (EFs) of the aerosol emitted from the combustion of toluene and
234 *n*-heptane as a function of combustion-chamber temperature. At the highest temperature (1035 °C), the
235 EFs of toluene were approximately 800 mg/kg-fuel, a factor of 20 larger than that of *n*-heptane
236 (approximately 40 mg/kg-fuel), demonstrating a strong dependence of aerosol formation on fuel
237 molecular structure. These findings indicate that, as expected, above 800 °C toluene has a larger
238 propensity for forming large organic molecules (including PAHs and their derivatives) that have low
239 enough volatilities to condense and form incipient soot particles, as further discussed in Section 3.3.



240

241 **Figure 2.** (a) Emission Factors of aerosols from toluene and *n*-heptane combustion as a function of
 242 combustion-chamber temperature. The error bars represent standard deviations from three separate
 243 experiments, with five measurements within each experiment. (b) Number distributions of aerosols
 244 from the combustion of toluene at 1035 °C, *n*-heptane at 1035 °C, and *n*-heptane at 290 °C, the peak
 245 temperature in the NTC region where aerosols were observed.

246 For both fuels, EFs exhibited a strong temperature dependence. Toluene EFs dropped by a factor of
 247 25 as the combustion-chamber temperature decreased from 1035 °C to 950 °C, and the aerosol
 248 emissions completely disappeared at temperatures below 750 °C. Similarly, aerosol emissions from *n*-
 249 heptane combustion disappeared at temperatures below 950 °C. However, at low temperatures (< 350
 250 °C), *n*-heptane combustion exhibited a sharp resurgence in aerosol emissions that was not observed
 251 with toluene, with EF peak of approximately 200 mg/kg-fuel at 290 °C. This rather striking two-stage
 252 aerosol formation directly reflects low-temperature ignition behavior, which is a trait of *n*-alkanes and
 253 is driven by the formation and reaction of peroxy radicals (ROO) that lead to several classes of
 254 intermediates, including cyclic ether isomers and alkene isomers, as further discussed in Section 3.2.
 255 Such reactions are not relevant in the oxidation of toluene largely due to the inability to form ROO
 256 because of the stability of the aromatic structure that creates high C–H bond energy (~112 kcal/mol) on
 257 phenyllic sites, which resist H-abstraction at lower temperatures.

258 The strong dependence of aerosol EFs on fuel molecular structure and combustion temperature
 259 highlights the potential importance of combustion conditions and types of fuel blends in dictating
 260 aerosol formation in engines. The results in Figure 2a suggest that relatively small differences in in-

261 cylinder temperature profiles can lead to large differences in aerosol emissions. Furthermore, our results
262 suggest that different fuel blends might have significantly different aerosol EF profiles.

263 Figure 2b shows number size distributions of the aerosol particles emitted from toluene combustion
264 at combustion-chamber temperature of 1035 °C and from *n*-heptane combustion at combustion-
265 chamber temperatures of 1035 °C and 290 °C. We note the emissions were diluted by clean air prior to
266 measurement (Figure 1). Therefore, the size distributions in Figure 2b were obtained by scaling the
267 SMPS measurements by the dilution factor in each experiment (66 for toluene and 16 for *n*-heptane).
268 The aerosol particles in all experiments were mostly ultrafine (< 100 nm), which is consistent with
269 aerosol size distributions measured in LTC engine emissions [2, 36] and indicates that the particles are
270 dominated by OA (incipient soot) with negligible contribution from BC (mature soot) [18].

271 3.2. Chemical kinetics modeling of species profiles

272 Species profiles of *n*-heptane and toluene were simulated at the conditions of the experiments using
273 the perfectly stirred reactor module in the ChemKin-Pro 19.2 program with the reaction mechanism of
274 Mehl et al. [53]. Table 2 shows the initial conditions used in the simulations. It is important to note that
275 this mechanism was developed to predict ignition delay times, not soot formation, the chemical
276 mechanisms for which differ substantially. Additional work is required to produce mechanisms capable
277 of describing ignition chemistry simultaneously with soot formation [68-72]. As shown in Figure 3a,
278 the depletion profile for *n*-heptane exhibits clear NTC (negative temperature coefficient) behavior
279 starting near ~325 °C, which is due to a shift in the balance of reactions derived from ROO from chain-
280 branching to chain-propagating and chain-inhibiting. The simulations also show the depletion of *n*-
281 heptane beginning at the lower end of the temperature range. In contrast, toluene mole fractions remain
282 unchanged until ~600 °C, above which significant depletion is evident in the mole fraction predictions
283 over a relatively narrow temperature range. Moreover, no NTC behavior is observed, which is
284 consistent with the diminished importance of ROO chemistry in toluene combustion.

285 **Table 2.** Initial mole fractions for reactants of each species and reactor conditions used in chemical
286 kinetics simulations.

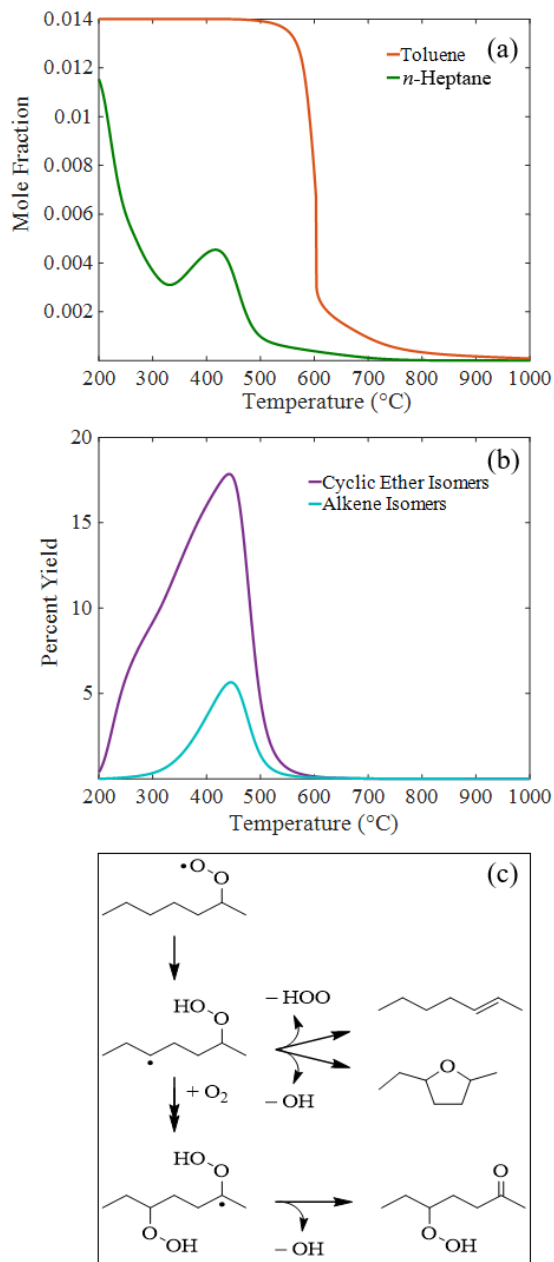
	toluene combustion	<i>n</i>-heptane combustion
Mole Fraction (fuel)	0.014	0.012
Mole Fraction (O ₂)	0.056	0.053
Mole Fraction (N ₂)	0.930	0.935
Residence Time (min.)	0.310	0.300
Temperature (°C)	200 – 1100	

287

288 Intermediates produced from peroxy radicals are major species in the NTC region. To examine the
 289 temperature dependence of partially oxidized species, mole fractions were also simulated for two
 290 classes of intermediates: cyclic ethers and isomers of heptene. The latter class includes 1-heptene, 2-
 291 heptene, 3-heptene, and 4-heptene, while the former comprises a total of ten cyclic ether isomers,
 292 including 2-methyl-5-ethyl tetrahydrofuran and 2-pentyloxirane. Based on the mole fraction results,
 293 percent yield calculations were conducted (Figure 3b) to quantify the extent to which the formation of
 294 the ROO-derived intermediates overlap with the temperature region where aerosol formation is
 295 observed (cf. Figure 2a). In the present context, the percent yield is a measure of the total amount of
 296 intermediates produced from ROO-mediated pathways, such as in Figure 3c, relative to the initial
 297 concentration of *n*-heptane (12000 ppm). As noted previously, the chemical kinetics mechanism used
 298 for the simulations excludes soot formation chemistry, which is a likely reason for the temperature
 299 dependence of the simulations differing from the experiments. However, as evident in Figure 3b, the
 300 two classes of intermediates are formed in abundance in the region where aerosols are produced in the
 301 experiments, which could explain the difference between the emissions trends in *n*-heptane versus
 302 toluene. More specifically, considering that ROO chemistry occurs in the combustion of *n*-heptane, and
 303 not toluene, it is plausible that the species produced in the NTC region where aerosols are observed
 304 experimentally are involved in the formation pathways of the aerosols.

305 Notably, the 13 species included in the mole fraction profiles in Figure 3b (10 cyclic ethers and 3
 306 heptene isomers) comprise only ~1% of the total number of reactions in the mechanism of Mehl et al.
 307 [53] (1389 species), yet account for ~20% of the gas-phase product formation in the NTC region of *n*-

308 heptane. Moreover, cyclic ethers may provide what effectively serves as the first ring required for
309 particle formation in low-temperature combustion, similar to that required for the HACA mechanism
310 [16] for high-temperature combustion, which is initiated via propargyl + propargyl, propargyl + allyl,
311 among other reactions to provide the first ring. The pathways that may unfold after the initial (cyclic
312 ether) ring are unclear. However, as cyclic ethers become oxidized and increasingly unsaturated, low-
313 temperature particle formation may follow a HACA-type mechanism with one or more oxygen atoms
314 embedded in polycyclic structures, the presence which may alter aerosol reactivity, physical properties,
315 and optical properties.



316

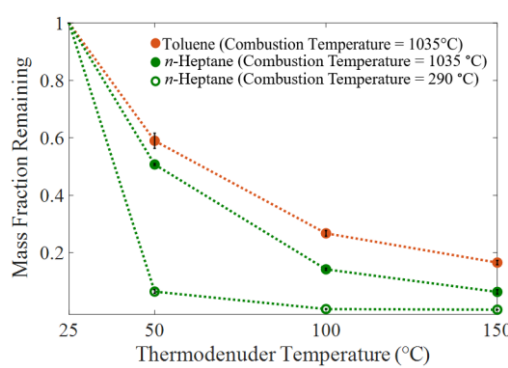
317 **Figure 3.** (a) ChemKin simulations of mole fractions of toluene and *n*-heptane conducted at 1 atm as a
 318 function of temperature. (b) Percent yields of cyclic ethers and conjugate alkenes derived from reactions
 319 of *n*-heptane-derived ROO radicals. (c) Reaction scheme of 2-heptylperoxy forming 2-heptene and 2-
 320 methyl-5-ethyltetrahydrofuran via QOOH decomposition and hept-2-one-5-hydroperoxy via second-
 321 O₂-addition. Combined, the yield through cyclic ether and alkene channels accounts for significant
 322 consumption of *n*-heptane in the region where organic aerosol is observed (cf. Figure 2a).

323

324 3.3. Volatility and molecular sizes

325 Figure 4 shows the aerosol mass fraction remaining (MFR) at different thermodenuder temperatures,
326 or thermograms. At a combustion-chamber temperature of 1035 °C, the thermogram of *n*-heptane-
327 combustion aerosol is steeper than that of toluene-combustion aerosol, indicating that the *n*-heptane-
328 combustion aerosol is more volatile. At the largest thermodenuder temperature (150 °C), MFR of
329 toluene-combustion aerosol was 0.17 compared to 0.06 for *n*-heptane-combustion aerosol. The aerosol
330 produced in the low-temperature region from *n*-heptane-combustion (290 °C; Figure 2a) evaporated
331 completely (i.e. MFR = 0) at thermodenuder temperature of 100 °C, indicating that it was significantly
332 more volatile than the aerosol produced by the same fuel at 1035 °C. These results suggest a strong
333 dependence of aerosol volatility on fuel type and combustion temperature.

334 Differences in aerosol volatility have implications to the atmospheric concentrations and lifecycle
335 of the aerosol species. Specifically, even for the same emission rate, a relatively low-volatility aerosol
336 would have higher atmospheric particle concentrations than a relatively high-volatility aerosol because
337 it is more resistant to evaporation upon dilution in the atmosphere [73]. On the other hand, the amounts
338 of semi-volatile organic compounds (SVOCs) that partition into the gas phase upon dilution in the
339 atmosphere would be higher for the high-volatility aerosol. SVOCs are efficient secondary organic
340 aerosol (SOA) precursors [74]. Thus, the high-volatility aerosol emissions can potentially lead to higher
341 levels of SOA than the low-volatility aerosol emissions.



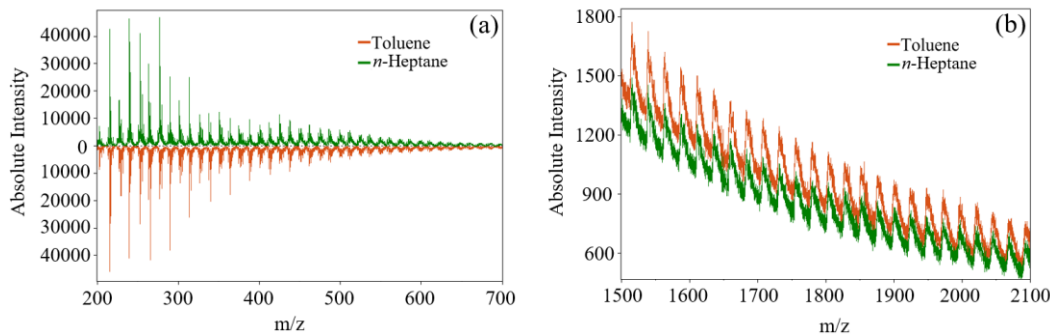
342

343 **Figure 4.** Thermograms showing mass fraction remaining (MFR) of toluene and *n*-heptane combustion
344 aerosols at different thermodenuder temperatures.

345 Mass spectra obtained from LDI-MS measurements for the aerosol emitted from toluene and *n*-
346 heptane combustion at combustion-chamber temperature of 1035 °C are shown in Figure 5a for $m/z <$
347 700 and Figure 5b for $1500 < m/z < 2100$. The mass spectra of molecules emitted from the two fuels
348 had similar signatures with sequences of major and minor peaks, each exhibiting spacings of 24 atomic
349 mass units with 12 atomic mass units separating the peaks of the two sequences. These signatures have
350 been previously observed in LDI-MS measurements of soot emissions [18, 61, 65] and are characteristic
351 of organic molecules in incipient soot undergoing growth by the hydrogen-abstraction acetylene-
352 addition (HACA) mechanism [16]. The similarity in mass spectra indicates that despite the difference
353 in molecular structure of the two fuels, the incipient soot emitted from their combustion is comprised
354 of species with similar molecular structure, likely dominated by polycyclic aromatic hydrocarbons
355 (PAHs) [16]. The peak intensities for $m/z < 700$ are of similar magnitude for the emissions from both
356 fuels. However, toluene-combustion aerosols had higher intensities in the large-molecular-size range
357 (Figure 5b), indicating that toluene-combustion aerosols had more abundance of large-molecular-size
358 species than aerosols emitted from *n*-heptane combustion. This is in-line with the finding that toluene-
359 combustion aerosols were less volatile than the *n*-heptane-combustion aerosols (Figure 4) because for
360 species with similar general molecular structure (e.g. the incipient soot produced in these experiments),
361 volatility decreases with increasing molecular size [75]. We note that due to differences in ionization
362 and desorption efficiencies of different molecules, the comparison shown in Figure 5 is qualitative.
363 Specifically, we expect the ionization and desorption, thus signal intensity [76], to decrease with
364 increasing molecular size. Therefore, we expect that in reality, the difference in abundance of molecules
365 on the large-end of the spectra to be more prominent than depicted in Figure 5b.

366 The aerosol emissions from *n*-heptane combustion in the low-temperature region did not exhibit any
367 discernible LDI-MS mass spectra. The LDI-MS technique requires that the sample absorbs the 337 nm
368 laser significantly enough in order for it to desorb. As discussed in Section 3.4, the aerosol emissions
369 from *n*-heptane combustion at low temperatures exhibited weak absorption in the visible spectrum, thus
370 it is likely they were not absorptive enough to be detected by LDI-MS. Based on their high volatility

371 (Figure 4), we expect these aerosols to be comprised of species with smaller molecular size than those
372 emitted in the high-temperature region.



373

374 **Figure 5.** LDI-MS spectra of aerosol emitted from toluene and *n*-heptane combustion at 1035 °C.

375 3.4. Light-absorption properties

376 The light-absorption properties of the aerosol emitted from the combustion of toluene (at
377 combustion-chamber temperature of 1035 °C) and *n*-heptane (at combustion-chamber temperature of
378 1035 °C and 290 °C) are depicted in Figure 6. Figure 6a shows the imaginary part of the refractive
379 indices at 422 nm, 532 nm, and 782 nm (k_{422} , k_{532} , and k_{782} , respectively) retrieved from optical closure
380 and Figure 6b shows the mass absorption cross-sections (MAC₄₂₂, MAC₅₃₂, and MAC₇₈₂) obtained from
381 normalizing the measured absorption coefficients by the mass concentration (Section 2.3). At
382 combustion-chamber temperature of 1035 °C, aerosols from both toluene and *n*-heptane combustion
383 exhibit significant absorption in the visible spectrum and are categorized as brown carbon (BrC). The
384 toluene-combustion aerosol is more absorptive (has larger k and MAC) than the *n*-heptane-combustion
385 aerosol, which is visually manifested as darker samples when collected on Teflon filters (Figure 6c).
386 However, k and MAC of *n*-heptane-combustion aerosol have a stronger wavelength dependence ($w = 7.6$
387 and AAE = 8.7) than toluene-combustion aerosol ($w = 4.1$ and AAE = 5.6). This inverse relation between
388 k and w (MAC and AAE) is consistent with previous reports showing that more absorptive BrC is
389 characterized with flatter absorption spectra [18, 22, 39, 77, 78].

390 We note that these findings, in conjunction with the differences in molecular sizes (Figure 5) and
391 volatility (Figure 4), are consistent with the brown-black continuum hypothesis that we have previously

introduced to describe the light-absorbing carbonaceous aerosols, including BrC and BC, generated via the soot-formation route in combustion [18]. As the soot-formation process progresses toward full maturation (BC formation), it produces incipient soot (or BrC) comprised of increasingly larger organic molecules that are less volatile and more light-absorbing (larger k and smaller w). Our results indicate that toluene-combustion BrC is further ahead in the soot-formation process than *n*-heptane-combustion BrC (closer to the BC-formation threshold) and is therefore darker, less volatile, and exhibits molecular size distributions skewed toward larger sizes than *n*-heptane-combustion BrC.

For *n*-heptane combustion at 290 °C, the emitted aerosol exhibited measurable absorption only at 422 nm (Figure 6a and 6b) and was thus barely visible when collected on a Teflon filter (Figure 6c). This indicates that unlike at the higher combustion temperature of 1035 °C, the low combustion temperature of 290 °C was not conducive for the formation of large-molecular-size PAHs that exhibit absorption spectra extending into the visible wavelengths. Based on the chemical kinetics modeling results (Section 3.2), the aerosols emitted at 290 °C are possibly comprised of cyclic ethers, which do not contain chromophores that are significantly absorptive at mid- and long-visible wavelengths.

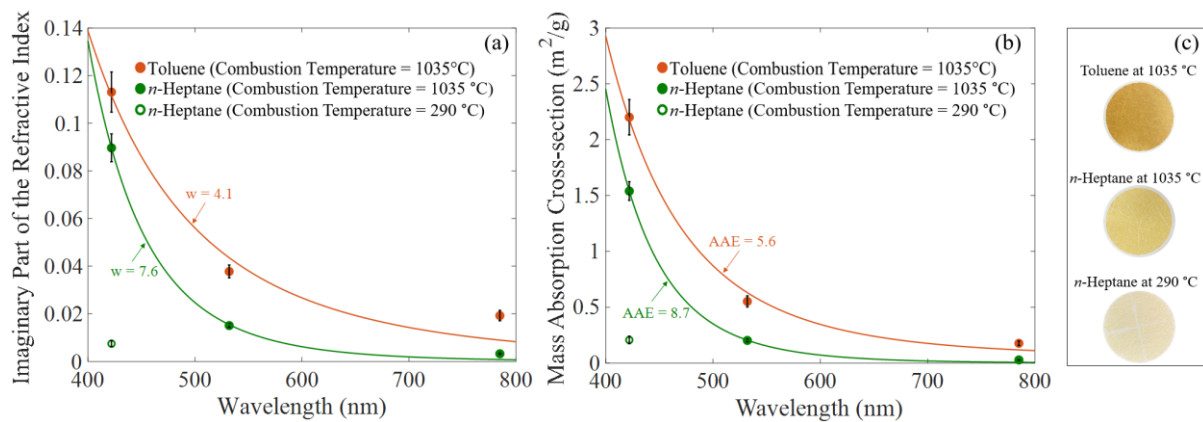


Figure 6. Light-absorption properties of aerosols emitted from toluene and *n*-heptane combustion. (a) Imaginary part of the refractive index (k) at different wavelengths. (b) Mass absorption cross section (MAC) at different wavelengths. Solid lines are power-law fits and the exponents are w and AAE, which represent the wavelength depends of k and MAC, respectively. The aerosol emitted from *n*-heptane combustion at 290 °C did not exhibit measurable absorption at 532 nm and 782 nm, thus light-absorption

412 properties are only reported at 422 nm (open green circles in panels (a) and (b)). (c) Pictures of filter
413 samples that visually illustrate the differences in optical properties of the aerosol emissions.

414 The BrC (incipient soot) emissions at the low-temperature combustion conditions in this study are
415 significantly less absorptive than the BC (mature soot) emitted at typical CDC or laboratory flame
416 conditions. Mature soot has $MAC_{532} \approx 8 \text{ g/m}^2$ and relatively flat wavelength dependence with $AAE \approx 1$
417 [15]. An important implication of this difference in light-absorption properties is that incipient soot
418 produced at low-temperature combustion conditions would not be accurately quantified using
419 techniques that rely on optical measurements tailored for mature soot, e.g. filter smoke number (FSN)
420 or microsoot sensor (MSS) [28, 29, 32, 33]. The MSS is a photoacoustic instrument that converts
421 absorption measurements at 880 nm to soot mass concentrations based on calibration against
422 combustion soot with high EC content (i.e. mature soot) [79]. Therefore, embedded in the reported MSS
423 mass concentrations is an assumption that the measured aerosol has the same MAC_{880} as mature soot
424 ($\approx 5 \text{ g/m}^2$). The aerosol emitted from toluene and *n*-heptane combustion at 1035 °C had MAC_{880} of 0.03
425 g/m^2 and 0.0025 g/m^2 , respectively, a factor of 152 and 1963 smaller than MAC_{880} of EC. Therefore,
426 their mass concentrations would be underestimated by the same factors if measured using a MSS. Such
427 large underestimation in mass concentrations of aerosol emissions from engines operated at LTC
428 conditions has been previously reported for FSN [32] and MSS [2]. Our findings provide support for
429 these reports and further indicate that optical absorption instruments are not suitable for quantifying
430 LTC aerosol emissions even if they are calibrated with aerosol emissions at LTC conditions. Unlike
431 mature soot which has relatively uniform light-absorption properties [21] regardless of emission source
432 (conventional diesel combustion, laboratory diffusion flames, etc.), the light-absorption properties of
433 incipient soot produced at LTC conditions can vary over several orders of magnitude depending on
434 combustion conditions (Figure 6), making it impossible to produce a calibration standard.

435 **4. Conclusions**

436 Using an atmospheric-pressure reactor controlled at a constant equivalence ratio and O_2/N_2 , we
437 investigated the effect of combustion temperature on the formation and physicochemical properties of
438 aerosols emitted from the combustion of toluene at *n*-heptane at temperatures between 200 °C and 1035

439 °C. Consistent with fuel reactivity versus temperature profiles predicted by ignition chemistry
440 simulations, aerosol emission factors from toluene combustion exhibited steep decrease with decreasing
441 combustion temperature, while the emission rates from *n*-heptane combustion exhibited steep decrease
442 with decreasing temperatures followed by resurgence that peaked at 290 °C. The physicochemical
443 properties of the aerosols varied with both fuel type and combustion temperature. At 1035 °C, toluene
444 combustion produced aerosols with molecular size distributions skewed to larger sizes compared to
445 aerosols emitted from *n*-heptane. The toluene-combustion aerosols were also less volatile and more
446 light-absorbing (darker), though both toluene-combustion and *n*-heptane-combustion aerosols are
447 categorized as brown carbon (BrC). For *n*-heptane combustion, the aerosols emitted at 290 °C were
448 significantly less light-absorbing and more volatile than those emitted at 1035 °C. The findings reported
449 here provide the first evidence for the strong dependence of aerosol formation at low-temperature
450 combustion conditions on ignition chemistry, particularly the two-stage aerosol formation in *n*-heptane
451 combustion that reflects its two-stage ignition chemistry behavior. They also highlight the importance
452 of further investigating the parameter space (fuel type and combustion conditions) associated with
453 aerosol emissions at LTC conditions in order to identify regions within this space that can potentially
454 minimize the emissions.

455 **Acknowledgments**

456 We thank the University of Georgia Proteomics and Mass Spectrometry Core Facility for performing
457 the LDI-MS analysis. Financial support was provided by the National Science Foundation, Division of
458 Atmospheric and Geospace Sciences (AGS-1748080) and the University of Georgia Interdisciplinary
459 Seed Grant Initiative.

460 **References**

- 461 [1] J. E. Dec and W. Hwang, "Characterizing the development of thermal stratification in
462 an HCCI engine using planar-imaging thermometry," *SAE International Journal of*
463 *Engines*, vol. 2, no. 1, pp. 421-438, 2009.
- 464 [2] M. Moses-DeBusk, S. J. Curran, S. A. Lewis, R. M. Connatser, and J. M. Storey,
465 "Impacts of Air-Fuel Stratification in ACI Combustion on Particulate Matter and
466 Gaseous Emissions," *Emission Control Science and Technology*, vol. 5, no. 3, pp. 225-
467 237, 2019.

468 [3] J. E. Dec, "Advanced compression-ignition engines—understanding the in-cylinder
469 processes," *Proceedings of the combustion institute*, vol. 32, no. 2, pp. 2727-2742,
470 2009.

471 [4] R. H. Stanglmaier and C. E. Roberts, "Homogeneous charge compression ignition
472 (HCCI): benefits, compromises, and future engine applications," *SAE transactions*, pp.
473 2138-2145, 1999.

474 [5] R. H. Thring, "Homogeneous-charge compression-ignition (HCCI) engines," SAE
475 Technical paper, 0148-7191, 1989.

476 [6] F. Zhao, T. N. Asmus, D. N. Assanis, J. E. Dec, J. A. Eng, and P. M. Najt, "Homogeneous
477 charge compression ignition (HCCI) engines," SAE Technical Paper, 2003.

478 [7] K. Epping, S. Aceves, R. Bechtold, and J. E. Dec, "The potential of HCCI combustion
479 for high efficiency and low emissions," SAE Technical Paper, 0148-7191, 2002.

480 [8] D. Splitter, R. Hanson, S. Kokjohn, and R. D. Reitz, "Reactivity controlled compression
481 ignition (RCCI) heavy-duty engine operation at mid-and high-loads with conventional
482 and alternative fuels," SAE Technical Paper, 0148-7191, 2011.

483 [9] R. D. Reitz and G. Duraisamy, "Review of high efficiency and clean reactivity
484 controlled compression ignition (RCCI) combustion in internal combustion engines,"
485 *Progress in Energy and Combustion Science*, vol. 46, pp. 12-71, 2015.

486 [10] D. Kang, A. Shah, T. Rockstroh, and S. Goldsborough, "Utilizing static autoignition
487 measurements to estimate intake air condition requirements for compression
488 ignition in a multi-mode engine-Application of Chemical Kinetic Modeling," SAE
489 Technical Paper, 0148-7191, 2019.

490 [11] E. A. Ortiz-Soto, G. A. Lavoie, M. S. Wooldridge, and D. N. Assanis, "Thermodynamic
491 efficiency assessment of gasoline spark ignition and compression ignition operating
492 strategies using a new multi-mode combustion model for engine system
493 simulations," *International Journal of Engine Research*, vol. 20, no. 3, pp. 304-326,
494 2019.

495 [12] A. K. Agarwal, A. P. Singh, and R. K. Maurya, "Evolution, challenges and path forward
496 for low temperature combustion engines," *Progress in Energy and Combustion
497 Science*, vol. 61, pp. 1-56, 2017.

498 [13] M. Han, "The effects of synthetically designed diesel fuel properties—cetane number,
499 aromatic content, distillation temperature, on low-temperature diesel combustion,"
500 *Fuel*, vol. 109, pp. 512-519, 2013.

501 [14] T. Kitamura, T. Ito, Y. Kitamura, M. Ueda, J. Senda, and H. Fujimoto, "Soot kinetic
502 modeling and empirical validation on smokeless diesel combustion with oxygenated
503 fuels," *SAE transactions*, pp. 945-963, 2003.

504 [15] T. C. Bond and R. W. Bergstrom, "Light absorption by carbonaceous particles: An
505 investigative review," *Aerosol science and technology*, vol. 40, no. 1, pp. 27-67, 2006.

506 [16] H. Wang, "Formation of nascent soot and other condensed-phase materials in
507 flames," *Proceedings of the Combustion institute*, vol. 33, no. 1, pp. 41-67, 2011.

508 [17] H. Michelsen, "Probing soot formation, chemical and physical evolution, and
509 oxidation: A review of in situ diagnostic techniques and needs," *Proceedings of the
510 Combustion Institute*, vol. 36, no. 1, pp. 717-735, 2017.

511 [18] R. Saleh, Z. Cheng, and K. Atwi, "The brown–black continuum of light-absorbing
512 combustion aerosols," *Environmental Science & Technology Letters*, vol. 5, no. 8, pp.
513 508-513, 2018.

514 [19] A. Laskin, J. Laskin, and S. A. Nizkorodov, "Chemistry of Atmospheric Brown Carbon,"
515 (in en), *Chemical Reviews*, vol. 115, no. 10, pp. 4335-4382, 2015/05/27/ 2015, doi:
516 10.1021/cr5006167.

517 [20] M. Andreae and A. Gelencsér, "Black carbon or brown carbon? The nature of light-
518 absorbing carbonaceous aerosols," 2006.

519 [21] T. C. Bond *et al.*, "Bounding the role of black carbon in the climate system: A
520 scientific assessment," *Journal of Geophysical Research: Atmospheres*, vol. 118, no.
521 11, pp. 5380-5552, 2013.

522 [22] R. Saleh, "From Measurements to Models: Toward Accurate Representation of
523 Brown Carbon in Climate Calculations," *Current Pollution Reports*, vol. 6, no. 2, pp.
524 90-104, 2020/06/01 2020, doi: 10.1007/s40726-020-00139-3.

525 [23] D. R. Worton *et al.*, "Lubricating oil dominates primary organic aerosol emissions
526 from motor vehicles," *Environmental science & technology*, vol. 48, no. 7, pp. 3698-
527 3706, 2014.

528 [24] B. R. Kumar and S. Saravanan, "Effects of iso-butanol/diesel and n-pentanol/diesel
529 blends on performance and emissions of a DI diesel engine under premixed LTC (low
530 temperature combustion) mode," *Fuel*, vol. 170, pp. 49-59, 2016.

531 [25] V. Soloiu *et al.*, "LTC (low-temperature combustion) analysis of PCCI (premixed
532 charge compression ignition) with n-butanol and cotton seed biodiesel versus
533 combustion and emissions characteristics of their binary mixtures," *Renewable
534 Energy*, vol. 123, pp. 323-333, 2018.

535 [26] R. M. Hanson, S. L. Kokjohn, D. A. Splitter, and R. D. Reitz, "An experimental
536 investigation of fuel reactivity controlled PCCI combustion in a heavy-duty engine,"
537 *SAE international journal of engines*, vol. 3, no. 1, pp. 700-716, 2010.

538 [27] C. S. Lee, K. H. Lee, and D. S. Kim, "Experimental and numerical study on the
539 combustion characteristics of partially premixed charge compression ignition engine
540 with dual fuel☆," *Fuel*, vol. 82, no. 5, pp. 553-560, 2003.

541 [28] M. Sellnau, W. Moore, J. Sinnamon, K. Hoyer, M. Foster, and H. Husted, "GDCI multi-
542 cylinder engine for high fuel efficiency and low emissions," *Sae international journal
543 of engines*, vol. 8, no. 2, pp. 775-790, 2015.

544 [29] M. Sellnau, M. Foster, W. Moore, J. Sinnamon, K. Hoyer, and W. Klemm, "Second
545 generation GDCI multi-cylinder engine for high fuel efficiency and US tier 3
546 emissions," *SAE International Journal of Engines*, vol. 9, no. 2, pp. 1002-1020, 2016.

547 [30] H. Liu, X. Bi, M. Huo, C.-f. F. Lee, and M. Yao, "Soot emissions of various oxygenated
548 biofuels in conventional diesel combustion and low-temperature combustion
549 conditions," *Energy & fuels*, vol. 26, no. 3, pp. 1900-1911, 2012.

550 [31] I. R. Fattah *et al.*, "Spray and combustion investigation of post injections under low-
551 temperature combustion conditions with biodiesel," *Energy & Fuels*, vol. 32, no. 8,
552 pp. 8727-8742, 2018.

553 [32] J. M. Storey *et al.*, "Evolution and current understanding of physicochemical
554 characterization of particulate matter from reactivity controlled compression
555 ignition combustion on a multicylinder light-duty engine," *International Journal of
556 Engine Research*, vol. 18, no. 5-6, pp. 505-519, 2017.

557 [33] S. Ciatti, M. Johnson, B. D. Adhikary, R. D. Reitz, and A. Knock, "Efficiency and
558 emissions performance of multizone stratified compression ignition using different
559 octane fuels," SAE Technical Paper, 0148-7191, 2013.

560 [34] Y. An, M. Jaasim, V. Raman, H. G. Im, and B. Johansson, "In-cylinder combustion and
561 soot evolution in the transition from conventional compression ignition (CI) mode to
562 partially premixed combustion (PPC) mode," *Energy & fuels*, vol. 32, no. 2, pp. 2306-
563 2320, 2018.

564 [35] W. F. Northrop, P. V. Madathil, S. V. Bohac, and D. N. Assanis, "Condensational
565 growth of particulate matter from partially premixed low temperature combustion
566 of biodiesel in a compression ignition engine," *Aerosol Science and Technology*, vol.
567 45, no. 1, pp. 26-36, 2011.

568 [36] G. Lucachick, S. Curran, J. Storey, V. Prikhodko, and W. F. Northrop, "Volatility
569 characterization of nanoparticles from single and dual-fuel low temperature
570 combustion in compression ignition engines," *Aerosol Science and Technology*, vol.
571 50, no. 5, pp. 436-447, 2016.

572 [37] J. Zádor, C. A. Taatjes, and R. X. Fernandes, "Kinetics of elementary reactions in low-
573 temperature autoignition chemistry," *Progress in energy and combustion science*,
574 vol. 37, no. 4, pp. 371-421, 2011.

575 [38] K. Johansson, M. Head-Gordon, P. Schrader, K. Wilson, and H. Michelsen,
576 "Resonance-stabilized hydrocarbon-radical chain reactions may explain soot
577 inception and growth," *Science*, vol. 361, no. 6406, pp. 997-1000, 2018.

578 [39] Z. Cheng, K. Atwi, T. Onyima, and R. Saleh, "Investigating the dependence of light-
579 absorption properties of combustion carbonaceous aerosols on combustion
580 conditions," *Aerosol Science and Technology*, vol. 53, no. 4, pp. 419-434, 2019.

581 [40] Z. Cheng *et al.*, "Discrepancies between brown carbon light-absorption properties
582 retrieved from online and offline measurements," *Aerosol Science and Technology*,
583 pp. 1-12, 2020.

584 [41] Z. Cheng *et al.*, "Evolution of the light-absorption properties of combustion brown
585 carbon aerosols following reaction with nitrate radicals," *Aerosol Science and
586 Technology*, vol. 54, no. 7, pp. 849-863, 2020/07/02 2020, doi:
587 10.1080/02786826.2020.1726867.

588 [42] M. Shahbakhti, A. Ghazimirsaid, and C. R. Koch, "Experimental study of exhaust
589 temperature variation in a homogeneous charge compression ignition engine,"
590 *Proceedings of the Institution of Mechanical Engineers, Part D: Journal of Automobile
591 Engineering*, vol. 224, no. 9, pp. 1177-1197, 2010, doi: 10.1243/09544070jauto1473.

592 [43] S. Williams, L. Hu, T. Nakazono, H. Ohtsubo, and M. Uchida, "Oxidation catalysts for
593 natural gas engine operating under HCCI or SI conditions," *SAE International Journal
594 of Fuels and Lubricants*, vol. 1, no. 1, pp. 326-337, 2009.

595 [44] T. Gordon *et al.*, "Secondary organic aerosol formation exceeds primary particulate
596 matter emissions for light-duty gasoline vehicles," *Atmospheric Chemistry and
597 Physics*, vol. 14, no. 9, pp. 4661-4678, 2014.

598 [45] Y. Ju, W. Sun, M. P. Burke, X. Gou, and Z. Chen, "Multi-timescale modeling of ignition
599 and flame regimes of n-heptane-air mixtures near spark assisted homogeneous
600 charge compression ignition conditions," *Proceedings of the Combustion Institute*,
601 vol. 33, no. 1, pp. 1245-1251, 2011.

602 [46] H. Machrafi, "Experimental validation of a kinetic multi-component mechanism in a
603 wide HCCI engine operating range for mixtures of n-heptane, iso-octane and
604 toluene: Influence of EGR parameters," *Energy conversion and management*, vol. 49,
605 no. 11, pp. 2956-2965, 2008.

606 [47] P. Hellier, N. Ladommato, R. Allan, and J. Rogerson, "Combustion and emissions
607 characteristics of toluene/n-heptane and 1-octene/n-octane binary mixtures in a
608 direct injection compression ignition engine," *Combustion and flame*, vol. 160, no.
609 10, pp. 2141-2158, 2013.

610 [48] T. W. Ryan and A. C. Matheaus, "Fuel Requirements for HCCI Engine Operation," *SAE
611 Transactions*, vol. 112, pp. 1143-1152, 2003. [Online]. Available:
612 www.jstor.org/stable/44742337.

613 [49] F. Contino, F. Foucher, C. Mounaïm-Rousselle, and H. Jeanmart, "Combustion
614 characteristics of tricomponent fuel blends of ethyl acetate, ethyl propionate, and
615 ethyl butyrate in homogeneous charge compression ignition (HCCI)," *Energy & fuels*,
616 vol. 25, no. 4, pp. 1497-1503, 2011.

617 [50] S. Zhong, M. Wyszynski, A. Megaritis, and D. Yap, "H. Xu, "Experimental Investigation
618 into HCCI Combustion Using Gasoline and Diesel Blended Fuels," SAE technical
619 paper," SAE 2005-01-3733, 2005.

620 [51] M. Christensen and B. Johansson, "Influence of mixture quality on homogeneous
621 charge compression ignition," *SAE transactions*, pp. 951-963, 1998.

622 [52] X. Lu, D. Han, and Z. Huang, "Fuel design and management for the control of
623 advanced compression-ignition combustion modes," *Progress in Energy and
624 Combustion Science*, vol. 37, no. 6, pp. 741-783, 2011.

625 [53] M. Mehl, W. J. Pitz, C. K. Westbrook, and H. J. Curran, "Kinetic modeling of gasoline
626 surrogate components and mixtures under engine conditions," *Proceedings of the
627 Combustion Institute*, vol. 33, no. 1, pp. 193-200, 2011.

628 [54] K. Atwi *et al.*, "Physicochemical properties and cytotoxicity of brown carbon
629 produced under different combustion conditions," *Atmospheric Environment*, vol.
630 244, p. 117881.

631 [55] P. H. McMurry, X. Wang, K. Park, and K. Ehara, "The relationship between mass and
632 mobility for atmospheric particles: A new technique for measuring particle density,"
633 *Aerosol Science & Technology*, vol. 36, no. 2, pp. 227-238, 2002.

634 [56] M. K. Donnelly and G. W. Mulholland, *Particle Size Measurements for Spheres with
635 Diameters of 50 nm to 400 nm*. US Department of Commerce, Technology
636 Administration, National Institute of ..., 2003.

637 [57] N. Tajima, N. Fukushima, K. Ehara, and H. Sakurai, "Mass range and optimized
638 operation of the aerosol particle mass analyzer," *Aerosol Science and Technology*,
639 vol. 45, no. 2, pp. 196-214, 2011.

640 [58] O. Schmid *et al.*, "Derivation of the density and refractive index of organic matter
641 and elemental carbon from closure between physical and chemical aerosol
642 properties," *Environmental science & technology*, vol. 43, no. 4, pp. 1166-1172, 2009.

643 [59] E. S. Cross *et al.*, "Laboratory and ambient particle density determinations using light
644 scattering in conjunction with aerosol mass spectrometry," *Aerosol Science and
645 Technology*, vol. 41, no. 4, pp. 343-359, 2007.

646 [60] D. A. Fischer and G. D. Smith, "A portable, four-wavelength, single-cell photoacoustic
647 spectrometer for ambient aerosol absorption," *Aerosol Science and Technology*, vol.
648 52, no. 4, pp. 393-406, 2018.

649 [61] K. Atwi *et al.*, "Physicochemical properties and cytotoxicity of brown carbon
650 produced under different combustion conditions," *Atmospheric Environment*, vol.
651 244, p. 117881, 2021.

652 [62] C. F. Bohren and D. R. Huffman, *Absorption and scattering of light by small particles*.
653 John Wiley & Sons, 2008.

654 [63] R. Saleh, A. Shihadeh, and A. Khlystov, "On transport phenomena and equilibration
655 time scales in thermodenuders," *Atmospheric Measurement Techniques*, vol. 4, no.
656 3, pp. 571-581, 2011.

657 [64] B. Apicella *et al.*, "Mass spectrometric analysis of large PAH in a fuel-rich ethylene
658 flame," *Proceedings of the Combustion Institute*, vol. 31, no. 1, pp. 547-553, 2007.

659 [65] A. Faccinetto, P. Desgroux, M. Ziskind, E. Therssen, and C. Focsa, "High-sensitivity
660 detection of polycyclic aromatic hydrocarbons adsorbed onto soot particles using
661 laser desorption/laser ionization/time-of-flight mass spectrometry: An approach to
662 studying the soot inception process in low-pressure flames," *Combustion and Flame*,
663 vol. 158, no. 2, pp. 227-239, 2011.

664 [66] A. Faccinetto, C. Focsa, P. Desgroux, and M. Ziskind, "Progress toward the
665 quantitative analysis of PAHs adsorbed on soot by laser desorption/laser
666 ionization/time-of-flight mass spectrometry," *Environmental science & technology*,
667 vol. 49, no. 17, pp. 10510-10520, 2015.

668 [67] B. Apicella, M. Alfè, A. Amoresano, E. Galano, and A. Ciajolo, "Advantages and
669 limitations of laser desorption/ionization mass spectrometric techniques in the
670 chemical characterization of complex carbonaceous materials," *International Journal
671 of Mass Spectrometry*, vol. 295, no. 1-2, pp. 98-102, 2010.

672 [68] A. J. Josephson, R. R. Linn, and D. O. Lignell, "Modeling soot formation from solid
673 complex fuels," *Combustion and Flame*, vol. 196, pp. 265-283, 2018.

674 [69] J. Appel, H. Bockhorn, and M. Frenklach, "Kinetic modeling of soot formation with
675 detailed chemistry and physics: laminar premixed flames of C2 hydrocarbons,"
676 *Combustion and flame*, vol. 121, no. 1-2, pp. 122-136, 2000.

677 [70] M. Mueller, G. Blanquart, and H. Pitsch, "Hybrid method of moments for modeling
678 soot formation and growth," *Combustion and Flame*, vol. 156, no. 6, pp. 1143-1155,
679 2009.

680 [71] M. Yen, V. Magi, and J. Abraham, "Modeling Soot Formation in Turbulent Jet Flames
681 at Atmospheric and High-Pressure Conditions," *Energy & Fuels*, vol. 32, no. 8, pp.
682 8857-8867, 2018.

683 [72] P. Akridis and S. Rigopoulos, "Modelling of soot formation in laminar diffusion flames
684 using a comprehensive CFD-PBE model with detailed gas-phase chemistry,"
685 *Combustion Theory and Modelling*, vol. 21, no. 1, pp. 35-48, 2017.

686 [73] N. M. Donahue, A. Robinson, C. Stanier, and S. Pandis, "Coupled partitioning,
687 dilution, and chemical aging of semivolatile organics," *Environmental science &
688 technology*, vol. 40, no. 8, pp. 2635-2643, 2006.

689 [74] Y. Zhao *et al.*, "Reducing secondary organic aerosol formation from gasoline vehicle
690 exhaust," *Proceedings of the National Academy of Sciences*, vol. 114, no. 27, pp.
691 6984-6989, 2017.

692 [75] N. M. Donahue, S. Epstein, S. N. Pandis, and A. L. Robinson, "A two-dimensional
693 volatility basis set: 1. organic-aerosol mixing thermodynamics," *Atmospheric
694 Chemistry and Physics*, vol. 11, no. 7, pp. 3303-3318, 2011.

695 [76] A. Cristadoro, H. J. Räder, and K. Müllen, "Clustering of polycyclic aromatic
696 hydrocarbons in matrix-assisted laser desorption/ionization and laser desorption
697 mass spectrometry," *Rapid Communications in Mass Spectrometry: An International*

698 *Journal Devoted to the Rapid Dissemination of Up-to-the-Minute Research in Mass*
699 *Spectrometry*, vol. 21, no. 16, pp. 2621-2628, 2007.

700 [77] C. D. McClure, C. Y. Lim, D. H. Hagan, J. H. Kroll, and C. D. Cappa, "Biomass-burning-
701 derived particles from a wide variety of fuels—Part 1: Properties of primary particles,"
702 *Atmospheric Chemistry and Physics*, vol. 20, no. 3, pp. 1531-1547, 2020.

703 [78] R. Saleh *et al.*, "Brownness of organics in aerosols from biomass burning linked to
704 their black carbon content," *Nature Geoscience*, vol. 7, no. 9, pp. 647-650, 2014.

705 [79] L. Durdina *et al.*, "Response of real-time black carbon mass instruments to mini-CAST
706 soot," *Aerosol Science and Technology*, vol. 50, no. 9, pp. 906-918, 2016.

707